JOURNAL OF PROPULSION AND POWER
Vol. 27, No. 2, March–April 2011

Rotordynamic Analysis of a 5-Kilonewton Thrust Gas Turbine by Considering Bearing Dynamics

Geraldo Creci,* João Carlos Menezes,† and João Roberto Barbosa‡
Instituto Tecnológico de Aeronáutica, 12228-900 São José dos Campos, Brazil
and
João Aparecido Corrá§
TGM Turbinas Ltda, 14175-000 Sertãozinho, Brazil

DOI: 10.2514/1.B34104

In this work, a full rotordynamic analysis is performed for a 5-kN thrust gas turbine while taking into account bearing stiffness and damping dynamics. The shaft of the studied single spool gas turbine is supported by a deep groove ball bearing and a squeeze film damper. The dynamic stiffness and damping coefficients of these two bearings are used in a finite element model belonging to a C^1-class formulation for the study of whirl speeds and unbalance responses. The first six modal orbits of the shaft are plotted at the most important frequencies, and a transient analysis is performed to simulate the transition of the system through resonance. As a result, the dynamic behavior of the studied rotor-bearing system is predicted, and vibration problems are avoided. A good agreement among the results could be verified in all numerical analyses.

Nomenclature

A	=	area of shaft cross section
C_{ij}	=	bearing damping coefficients
$[C]$	=	damping matrix
D	=	dissipation function for a shaft element
E	=	Young's modulus of the shaft material
$\{F\}$	=	vector of external forces
G	=	shear modulus of the shaft material
$[G]$	=	gyroscopic matrix
I	=	second moment of inertia of the shaft
I_d, I_p	=	diameter and polar mass moments of inertia
K_{ij}	=	bearing stiffness coefficients
$[K]$	=	stiffness matrix
k	=	shear coefficient, $k = 6(1+\nu)/(7+6\nu)$
l	=	length of the shaft element
$[M]$	=	mass matrix
$N_i(s)$	=	one-dimensional quadratic Lagrangian shape function
$N_t(s)$	=	translational shape function matrix
$N_r(s)$	=	rotational shape function matrix
n	=	number of nodes per element
P	=	strain energy function for a shaft element
$\{q\}$	=	nodal displacement vector
s	=	axial distance within an element
T	=	shaft kinetic energy
t	=	time
U	=	shaft potential energy
(V, W)	=	translational displacements in y and z
(V_b, W_b)	=	components due to bending deformations
(V_s, W_s)	=	components due to shear deformations
x, y, z	=	fixed reference frame of the rotor
Γ	=	small angle rotation about the z-axis
η_H	=	hysteretic shaft material damping coefficient
η_V	=	viscous shaft material damping coefficient
ρ	=	shaft material mass density
ν	=	Poisson's ratio
Φ	=	small angle rotation about the y-axis
φ	=	rotor-bearing system angular displacement
Ω	=	rotational speed of the shaft
ω	=	spin rotor frequency

Superscripts

b	=	bearing
e	=	element
T	=	transpose
$\dot{}$	=	differentiation with respect to time
$'$	=	differentiation with respect to axial distance

I. Introduction

A FULL rotordynamic analysis is mandatory to avoid vibration resonance for a gas turbine operating at high speed. Critical speeds are defined as coincidences of the shaft rotating speed and the rotating natural frequencies of the rotor-bearing system. Because catastrophic failure occurs at critical speeds due to resonance, critical speeds are designed to be sufficiently separated from the operating speed range. Determination of instability threshold and unbalance system responses are also subjects of major concern.

There are several numerical approximations for vibration analysis of rotor-bearing systems. The most popular approach, which is particularly well suited for modeling large scale and complicated systems, is the finite element method. In view of this fact, Kalita and Kakoty [1] presented an analysis of whirl speeds for rotor-bearing systems supported on fluid film bearings. The presence of half-frequency whirling, which could potentially cause subharmonic instabilities in the system, was observed in their analysis. Chiang et al. [2] analyzed dual-rotor systems that considered the effects of the high-speed and low-speed shaft speed ratios on critical speeds. Their models were analyzed to predict natural frequencies, produce critical speed maps, and estimate bearing stiffnesses. Jeon et al. [3] used a three-dimensional finite element method to perform critical speed analysis of a 30-ton thrust demonstrator turbopump while considering the casing structural flexibility. They found that the effect of the casing structural flexibility reduced the critical speeds of the turbopump. Combescure and Lazarus [4] presented a comparison of the results given by analyses performed in a rotating frame and analyses performed with beam elements with finite element

Received 6 September 2010; accepted for publication 7 October 2010. Copyright © 2010 by the American Institute of Aeronautics and Astronautics, Inc. All rights reserved. Copies of this paper may be made for personal or internal use, on condition that the copier pay the $10.00 per-copy fee to the Copyright Clearance Center, Inc., 222 Rosewood Drive, Danvers, MA 01923; include the code 0748-4658/11 and $10.00 in correspondence with the CCC.

*Ph.D. Student, Sponsored by CAPES, Structures and Dynamics Division, ITA-EIM; gcreci@ita.br (Corresponding Author).
†Associate Professor, Structures and Dynamics Division, ITA-EIM.
‡Associate Professor, Propulsion and Power Division, ITA-EIM.
§Senior Engineer, Computer-Aided Design Division, TGM.

modeling. The resulting modeling approach was applied to the analysis of a gas turbine modular helium reactor power conversion unit.

In this work, a full rotordynamic analysis is performed for a single spool gas turbine designed for unmanned aerial vehicle applications. Figure 1 shows a cross-section view of the gas turbine designed to produce 5-kN of thrust at 469.17 Hz. The gas turbine is composed of a five-stage axial compressor, an annular combustion chamber, and a single-stage turbine rotor. Excitation frequencies can come from a variety of sources. The most critical is the mass unbalance of the rotor at frequency ω. Coupling misalignments give rise to an excitation frequency of 2ω. Blades, vanes, the nozzle, the diffuser, and other devices produce excitation frequencies of $s\omega$, where s is the number of blades, vanes and so on. Bearing excitation sources produce subharmonic excitation frequencies of 0.5ω.

The rotordynamic behavior of the studied gas turbine is investigated by taking into account the dynamic stiffness and damping coefficients of the bearings. The coefficients are used with a finite element model belonging to a C^1-class formulation for the study of whirl speeds and unbalance response analyses. A transient analysis is performed to evaluate the transition of the system through resonance. Vibration amplitudes are evaluated during turbine startup and when it is operating in steady state conditions. At the end of the paper, a spectral map plot is presented to identify possible vibration problems when considering excitation frequencies from 0 to 500 Hz.

II. Finite Element Formulation

The configuration of a simple rotor-bearing system is illustrated in Fig. 2. We assumed that, as compared with the translational motions, the axial motion is small enough to be reasonably neglected. A typical cross-section of the shaft located at a distance s from the left end, in a deformed state, can be described by the translations $V(s,t)$ and $W(s,t)$ in the y- and z-directions as well as the small rotations $\Phi(s,t)$ and $\Gamma(s,t)$ about the y- and z-axes. The relationships can be expressed as

$$V(s,t) = V_b(s,t) + V_s(s,t) \tag{1a}$$

$$W(s,t) = W_b(s,t) + W_s(s,t) \tag{1b}$$

$$\Phi(s,t) = -\frac{\partial W_b(s,t)}{\partial s} \tag{1c}$$

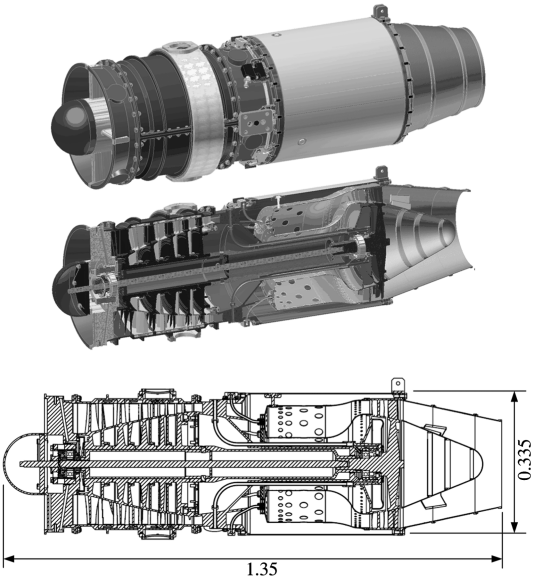

Fig. 1 Cross-section view of the studied single spool gas turbine. Dimensions are in meters.

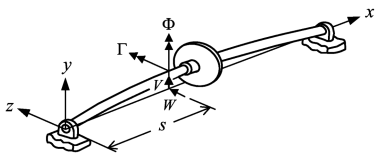

Fig. 2 Displacement variables and coordinate system of a rotor-bearing system.

$$\Gamma(s,t) = \frac{\partial V_b(s,t)}{\partial s} \tag{1d}$$

where V_b, V_s, and W_b, W_s are translations due to bending and shear in the y- and z-directions, respectively. The potential energy U^e of a shaft element of length l, including the elastic bending and shear deformation energy, can be expressed as

$$U^e = \frac{1}{2}\int_0^l EI\{(\Phi')^2 + (\Gamma')^2\}\,\mathrm{d}s + \frac{1}{2}\int_0^l kGA\{(V_s')^2 + (W_s')^2\}\,\mathrm{d}s \tag{2}$$

where

$$V_s' = \frac{\partial V}{\partial s} - \Gamma \tag{3a}$$

$$W_s' = \frac{\partial W}{\partial s} + \Phi \tag{3b}$$

are the shear strains. The kinetic energy T^e of a shaft element rotating at a constant speed Ω, including the translational and rotational forms, is given by

$$T^e = \frac{1}{2}\int_0^l \rho A\{(\dot{V})^2 + (\dot{W})^2\}\,\mathrm{d}s + \frac{1}{2}\int_0^l I_d\{(\dot{\Phi})^2 + (\dot{\Gamma})^2\}\,\mathrm{d}s - \int_0^l \Omega I_p \dot{\Gamma}\Phi\,\mathrm{d}s + \frac{1}{2}\int_0^l \Omega^2 I_p\,\mathrm{d}s \tag{4}$$

In the finite element method, the continuous displacement field can be approximated in terms of the discretized generalized displacements of the element nodes. Therefore, the displacement field internal to an element labeled e could be approximated as

$$\{V(s,t), W(s,t), \Phi(s,t), \Gamma(s,t)\} = \sum_{i=1}^{n} N_i(s)\{V_i, W_i, \Phi_i, \Gamma_i\} \tag{5}$$

or in a matrix form as

$$\begin{Bmatrix} V \\ W \end{Bmatrix} = [N_t(s)]\{q^e\} \tag{6}$$

$$\begin{Bmatrix} \Phi \\ \Gamma \end{Bmatrix} = [N_r(s)]\{q^e\} \tag{7}$$

where n is the number of nodes per element, $N_i(s)$ is the one-dimensional quadratic Lagrangian shape function, $\{q^e\}^T = \{V_1, W_1, \Phi_1, \Gamma_1, \ldots, V_n, W_n, \Phi_n, \Gamma_n\}$ is the nodal displacement vector, and $[N_t(s)]$ and $[N_r(s)]$ are the translational and rotational shape function matrices, respectively. From Eqs. (6) and (7), the shear strains are then related by the nodal displacement vector $\{q^e\}$ as

$$\begin{Bmatrix} V_s' \\ W_s' \end{Bmatrix} = ([N_t'] - [N][N_r])\{q^e\} \equiv [N_u(s)]\{q^e\} \tag{8a}$$

where

$$[N] = \begin{bmatrix} 0 & 1 \\ -1 & 0 \end{bmatrix} \tag{8b}$$

$$[N_u(s)] = [N_t'] - [N][N_r] \tag{8c}$$

With the aid of Eqs. (6), (7), and (8a), the element potential energy U^e and the element kinetic energy T^e can be rewritten in terms of the nodal displacement vector $\{q^e\}$ as, respectively,

$$U^e = \frac{1}{2}\{q^e\}^T([K_b^e] + [K_s^e])\{q^e\} \equiv \frac{1}{2}\{q^e\}^T[K^e]\{q^e\} \tag{9}$$

and

$$T^e = \frac{1}{2}\{\dot{q}^e\}^T([M_T^e] + [M_R^e])\{\dot{q}^e\} - \Omega\{\dot{q}^e\}^T[H^e]\{q^e\} + \frac{1}{2}I_p l\Omega^2 \tag{10}$$

where

$$[K_b^e] = \int_0^l [N_r']^T EI[N_r']\,\mathrm{d}s \tag{11a}$$

$$[K_s^e] = \int_0^l [N_u]^T kGA[N_u]\,\mathrm{d}s \tag{11b}$$

$$[M_T^e] = \int_0^l [N_t]^T \rho A[N_t]\,\mathrm{d}s \tag{11c}$$

$$[M_R^e] = \int_0^l [N_r]^T I_d[N_r]\,\mathrm{d}s \tag{11d}$$

$$[H^e] = \int_0^l I_p[N_r]^T \begin{bmatrix} 0 & 0 \\ 1 & 0 \end{bmatrix}[N_r]\,\mathrm{d}s \tag{11e}$$

A. Incorporation of Internal Damping

Zorzi and Nelson [5] considered the combined effects of both viscous and hysteretic internal damping in their finite element formulation of the rotor-bearing system. Using η_V and η_H to denote the viscous damping coefficient and the hysteretic loss factor of the shaft material, respectively, the strain energy dP^e and the dissipation function dD^e for an infinitesimal element, can be expressed as

$$dP^e = \frac{1}{2}EI\begin{Bmatrix} \Phi' \\ \Gamma' \end{Bmatrix}^T [\eta]\begin{Bmatrix} \Phi' \\ \Gamma' \end{Bmatrix}\mathrm{d}s \tag{12}$$

$$dD^e = \frac{1}{2}\eta_V EI\begin{Bmatrix} \dot{\Phi}' \\ \dot{\Gamma}' \end{Bmatrix}^T \begin{Bmatrix} \dot{\Phi}' \\ \dot{\Gamma}' \end{Bmatrix}\mathrm{d}s \tag{13}$$

where

$$[\eta] = \begin{bmatrix} \eta_a & \eta_b \\ -\eta_b & \eta_a \end{bmatrix} \tag{14a}$$

$$\eta_a = \frac{1 + \eta_H}{\sqrt{1 + \eta_H^2}} \tag{14b}$$

$$\eta_b = \frac{\eta_H}{\sqrt{1 + \eta_H^2}} + \Omega\eta_V \tag{14c}$$

Integrating Eqs. (12) and (13) over the whole length of the element gives the following equations for the strain energy and the shaft element dissipation function with internal viscous and hysteretic damping

$$P^e = \frac{1}{2}\eta_a\{q^e\}^T[K_b^e]\{q^e\} + \frac{1}{2}\eta_b\{q^e\}^T[K_d^e]\{q^e\} \tag{15}$$

$$D^e = \frac{1}{2}\eta_v\{\dot{q}^e\}^T[K_b^e]\{\dot{q}^e\} \tag{16}$$

where

$$[K_d^e] = \int_0^l EI[N_r']^T[N][N_r']\,\mathrm{d}s \tag{17}$$

For a finite shaft element with internal damping, the potential energy P^e and the dissipation function D^e, which both take into account the effect of shear deformations, become

$$P^e = \frac{1}{2}\eta_a\{q^e\}^T[K^e]\{q^e\} + \frac{1}{2}\eta_b\{q^e\}^T[K_c^e]\{q^e\} \tag{18}$$

$$D^e = \frac{1}{2}\eta_v\{\dot{q}^e\}^T[K^e]\{\dot{q}^e\} \tag{19}$$

where

$$[K^e] = [K_b^e] + [K_s^e] \tag{20}$$

$$[K_c^e] = [K_d^e] + \int_0^l kGA[N_u]^T[N][N_u]\,\mathrm{d}s \tag{21}$$

Using Hamilton's principle, the following matrix motion equation for the finite rotating shaft element is obtained

$$\begin{aligned}([M_T^e] + [M_R^e])\{\ddot{q}^e\} + (\eta_V[K^e] - \Omega[G^e])\{\dot{q}^e\} \\ + (\eta_a[K^e] + \eta_b[K_c^e])\{q^e\} = \{F^e\}\end{aligned} \tag{22}$$

where

$$[G^e] = [H^e] - [H^e]^T \tag{23}$$

B. Influence of the Bearings

The classic linearized model with eight spring and damping coefficients is used to model the bearings in the present work. In this model, the forces at each bearing are assumed to obey the governing equations of the following form

$$\begin{bmatrix} C_{yy} & C_{yz} \\ C_{zy} & C_{zz} \end{bmatrix}\{\dot{q}^b\} + \begin{bmatrix} K_{yy} & K_{yz} \\ K_{zy} & K_{zz} \end{bmatrix}\{q^b\} = \{F^b\} \tag{24}$$

where $\{q^b\} = \{\,V \quad W\,\}^T$ is the bearing displacement vector, C_{ij} and K_{ij} are the bearing damping and stiffness coefficients, respectively, and $\{F^b\}$ is the vector of bearing forces. In this work, the bearing stiffness and damping coefficients vary significantly as a function of the rotor speed. The terms of the matrices are stored in tables to be used according to the rotational speed of the rotor at the current solution step.

C. System Equations of Motions

The motion equations of the complete system can be obtained by assembling the contribution of each element motion equation [6,7]. The resultant system equation becomes

$$[M]\{\ddot{q}\} + ([C_b] + \Omega[G])\{\dot{q}\} + ([K_s] + [K_b])\{q\} = \{F\} \tag{25}$$

where $[M]$, $[G]$, $[K]$ are the assembled mass, gyroscopic and stiffness matrix of the system, respectively, and $[C_b]$ and $[K_b]$ are the bearing damping and stiffness matrices, respectively. The forcing vector $\{F\}$ contains all the forcing functions, such as synchronous excitations due to mass unbalance, shaft bow, skew discs, constant gravity loads, and static loads.

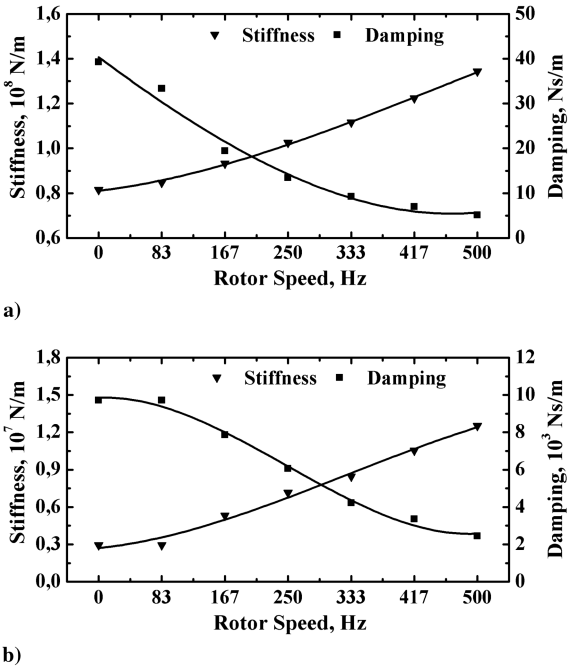

Fig. 3 Dynamic coefficients of the bearings: a) a lubricated deep groove ball bearing (front bearing) and b) a squeeze film damper (rear bearing).

In many applications, such as the one presented here, it is necessary to study the rotor-bearing system during transition through resonance. In this situation, the angular speed ($\Omega = \dot{\varphi}$) is no longer a constant but a function of time. The governing motion equations for a variable rotational speed system can be written as [8]

$$[M]\{\ddot{q}\} + ([C_b] + \dot{\varphi}[G])\{\dot{q}\} + ([K_s] + [K_b] + \ddot{\varphi}[G])\{q\} = \dot{\varphi}^2\{F_1\} + \ddot{\varphi}\{F_2\} \tag{26}$$

where all the damping and stiffness terms are in the damping and stiffness matrices. Two more terms introduced by using Lagrange's equation that derives the governing equations are the circulatory matrix $\ddot{\varphi}[G]$ and forcing function $\ddot{\varphi}\{F_2\}$. The vectors $\{F_1\}$ and $\{F_2\}$ are functions of $(\varphi, \dot{\varphi})$ and $(\varphi, \ddot{\varphi})$, respectively. They primarily result from mass unbalance and disc skew.

Table 1 Stiffness and damping coefficients of the bearings

	Front bearing		Rear bearing	
Rotor speed, Hz	Stiffness	Damping	Stiffness	Damping
	N/m	Ns/m	N/m	Ns/m
0	1.37×10^7	39.3	2.94×10^6	9719.7
83.33	1.37×10^7	33.4	2.94×10^6	9719.7
167.67	1.37×10^7	19.4	5.30×10^6	7855.7
250	1.37×10^7	13.5	7.16×10^6	6055.9
333.33	1.37×10^7	9.3	8.44×10^6	4216.1
416.67	1.37×10^7	7.0	10.5×10^6	3352.2
500	1.37×10^7	5.1	12.5×10^6	2441.2

[a]Note: $K_{yy} = K_{zz}$ and $C_{yy} = C_{zz}$.

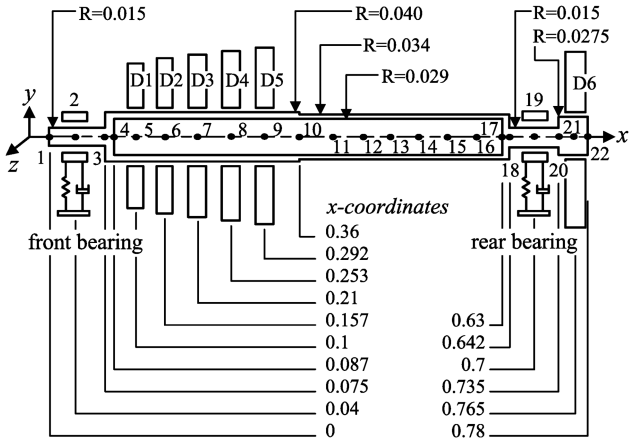

Fig. 4 Rotor-bearing model of the studied gas turbine. All dimensions are in meters.

III. Rotordynamic Model

The shaft of the studied gas turbine is supported by two bearings: a lubricated deep groove ball bearing (front bearing) and an unsealed squeeze film damper (rear bearing). In the works of Creci et al. [9,10], the stiffness and damping coefficients of these two bearings are presented as a function of the rotor speed. Figure 3a shows the dynamic coefficients of the deep groove ball bearing calculated using elastohydrodynamic lubrication theory. This ball bearing is mounted on a vibration absorber element, which has a stiffness of 1.37×10^7 N/m for all rotor speeds. Therefore, the front bearing is characterized by the stiffness of the vibration absorber element and the damping values of the lubricated ball bearing. The rear bearing is an unsealed squeeze film damper with a circumferential feeding groove. The geometric dimensions of the feeding groove and its interactions with the two oil film lands are taken into account to determine the dynamic coefficients of the damper. Figure 3b shows the dynamic stiffness and damping coefficients of the squeeze film damper. The stiffness and damping cross-coupled terms for both bearings are considered to be null. Table 1 shows the numerical values used in the calculations.

Figure 4 shows a schematic model of the studied rotor-bearing system with its main nodes. The shaft is made of AISI 4340 steel. The Young's modulus of AISI 4340 steel is 205 GPa, the Poisson's ratio is 0.29, and the density is 7850 kg/m^3. The discs are made of different materials to withstand the high gradient of mechanical and thermal loads. Table 2 shows the main physical and geometric properties of the discs. All discs are subjected to high centrifugal loads. The first three discs of the axial compressor are made of aluminum alloys. The fourth and fifth discs are made of titanium alloy because the temperatures over these discs are significantly higher. The sixth disc is the free turbine rotor, which is made of inconel alloy to withstand the high temperature loads from the post-combustion gases.

The finite element model was developed using Ansys® Parametric Design Language (APDL). The effects of rotary inertia, gyroscopic moments, axial loads, shear deformations, internal viscous, and hysteretic damping are included in the formulations, as shown in the previous section. All elements in the model have 4 degrees of freedom at each node. These include translations in the nodal y- and z-directions and rotations about the nodal y- and z-axes. The disc

Table 2 Physical and geometric disc properties

DISCS	D1	D2	D3	D4	D5	D6
Material	Al7178-T6	Al7178-T6	Al2024-T8	Ti-6Al-4V	Ti-6Al-4V	In713LC
Young's modulus, GPa	71.7	71.7	72.4	113.8	113.8	163.3
Density, kg/m^3	2830	2830	2870	4430	4430	8000
Poisson's ratio	0.33	0.33	0.33	0.342	0.342	0.382
Width, m	0.02	0.02	0.02	0.02	0.02	0.03
Inner diameter, m	0.08	0.08	0.08	0.08	0.08	0.055
Outer diameter, m	0.19	0.21	0.23	0.24	0.25	0.025

Table 3 Logarithmic decrements of the studied rotor-bearing system

Rotor speed, Hz	1FW mode	1BW mode	2FW mode	2BW mode	3FW mode	3BW mode
55.56	5.0437	5.2713	0.2024	0.0216	0.8447	0.8903
111.11	3.3526	3.8727	0.4609	0.0234	0.7276	0.7742
166.67	1.0670	2.4758	1.3331	0.0453	0.6332	0.5997
222.22	0.3705	1.7818	1.3666	0.0743	0.5428	0.4473
277.78	0.1605	1.2929	1.0972	0.1012	0.4522	0.3222
333.33	0.0779	0.9097	0.8126	0.1171	0.3563	0.2216
388.89	0.0419	0.6765	0.6255	0.1460	0.3253	0.1705
444.44	0.0256	0.4636	0.4822	0.1671	0.2886	0.1283
500	0.0171	0.3288	0.3251	0.1720	0.2445	0.0934

elements are elastic straight uniaxial elements with tension compression, torsion and bending capabilities. The front and rear bearings are modeled using matrix elements, which have an undefined geometry but an elastic kinematic response that can be specified by stiffness and damping coefficients as a function of the rotor speed.

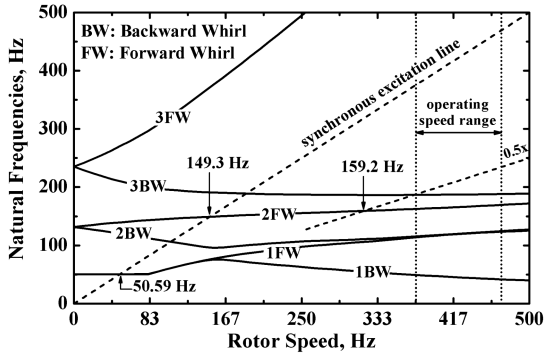

Fig. 5 Campbell diagram of the studied rotor-bearing system.

IV. Results and Discussion

The numerical analyses were performed considering a speed range from 0 to 500 Hz. According to the design specifications, the operating speed range of the rotor-bearing system ranges from 375.33 to 469.17 Hz, which is 80–100% of the maximum allowable speed. Figure 5 shows the Campbell diagram of the system. Two critical speeds are of major concern: the 1FW mode at 50.59 Hz and the 2FW mode at 149.3 Hz. We also observed that the 3FW mode varies drastically with increasing rotor speed. As shown in Table 3, no instability occurs when the rotor speed is below 500 Hz, since all logarithmic decrements are positive. It is well known that internal damping can destabilize a rotor, and the hysteretic damping model seems to occasionally predict an incorrect instability range [11]. Figure 6 qualitatively shows the first six modal orbits of the shaft plotted at the critical frequencies with respect to the synchronous excitation line.

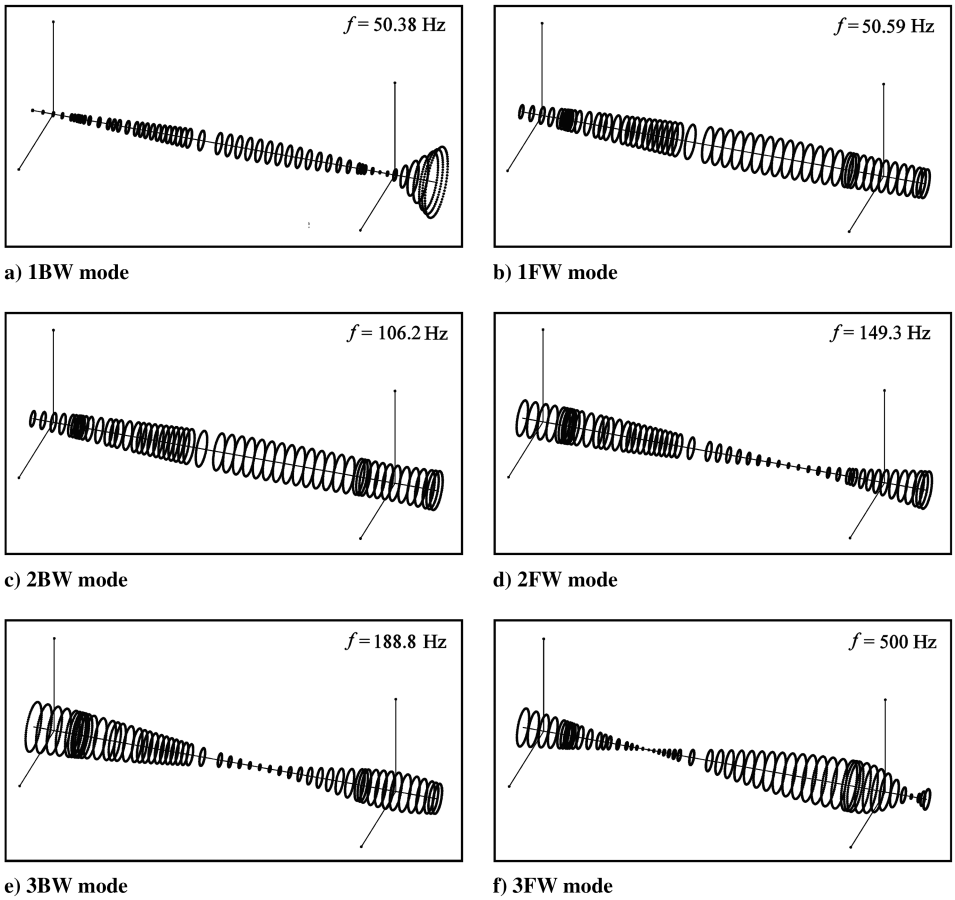

a) 1BW mode **b) 1FW mode**

c) 2BW mode **d) 2FW mode**

e) 3BW mode **f) 3FW mode**

Fig. 6 Modal orbits of the shaft plotted at the critical frequencies of the system with respect to the synchronous excitation line.

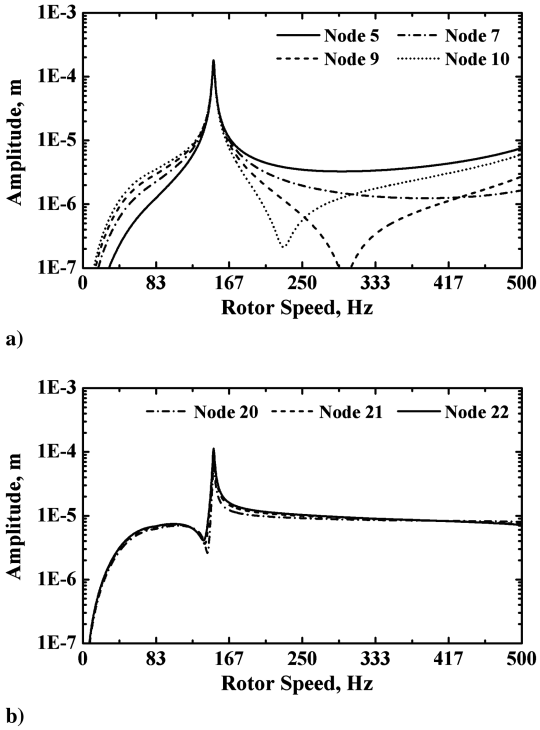

Fig. 7 Unbalance responses at specific nodes of the model: a) nodes of the five-stage axial compressor and b) nodes of the free turbine rotor.

In the numerical analyses presented here, we used a mass unbalance of 1×10^{-4} kg · m situated at node 21 of the finite element model. Figure 7 shows the unbalance responses of the studied rotor-bearing system evaluated at several nodes. Because the bearings are symmetric, only the forward modes are excited. We observe that the second critical speed (the 2FW mode at 149.3 Hz) is the most troublesome. The first critical speed (1FW mode at 50.59 Hz) is drastically attenuated by the damping performance of the squeeze film damper.

The vibration amplitudes were analyzed in both the five-stage axial compressor and the free turbine rotor because the tip blade clearances of these components are defined to be as small as possible for maximum fluid dynamic efficiency. The vibration amplitudes do not reach 6 μm for the five-stage axial compressor, or 9 μm for the free turbine rotor, considering the operating speed range from 375.33 to 469.17 Hz. However, the unbalance responses due to the second critical speed can reach 178 μm for the five-stage axial compressor and 104 μm for the free turbine rotor.

A transient analysis was performed to simulate the transition of the system through resonance. We assumed a linear acceleration law followed by a constant speed of rotation. The angular acceleration of the rotor is 314.15 rad/s^2. Figure 8 shows the displacement

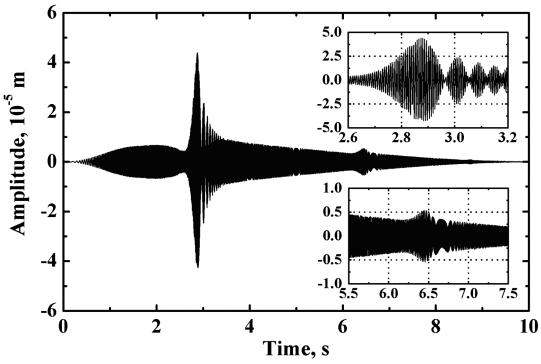

Fig. 8 Transition of the studied rotor-bearing system through resonance. The displacements are evaluated in the *y*-direction at node 21.

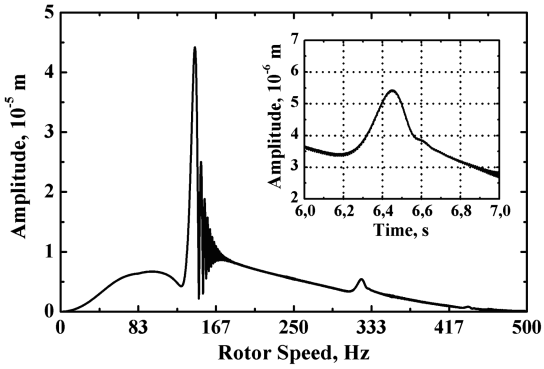

Fig. 9 Total displacements at node 21 during transition of the system through resonance.

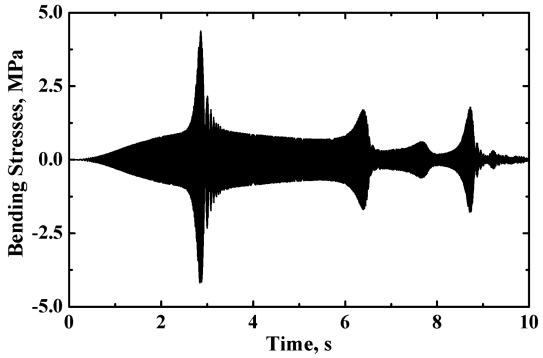

Fig. 10 Bending stresses evaluated at node 20 during system transition through resonance.

responses in the *y*-direction at node 21 for a 10-second total simulation time. Figure 9 shows the total displacements at node 21, considering the effects of horizontal and vertical displacements. A small peak appears in the solution about 6.45 seconds after the gas turbine startup. This amplitude peak relates to the 2FW mode at 159.2 Hz, as can be seen in the Campbell diagram shown in Fig. 5. This half-frequency whirling happens due to the high damping performance of the squeeze film damper because this amplitude peak disappears when lower damping values are used.

The alternated bending stresses were evaluated at specific points of the shaft. From Fig. 6, one can note that node 20 is located at the most critical region of the shaft, after the rear bearing and because of the free turbine rotor. Figure 10 shows the calculated bending stresses at this node during the transition of the system through resonance. As can be noted, low stress values were found throughout the transient phase. Figure 11 shows a spectral map plot of the studied rotor-bearing system. In this analysis, the rotor speed varies from 0 to 500 Hz with 50 substeps, and the excitation frequencies vary from 0 to 500 Hz with 250 substeps. The vibration amplitudes are calculated at node 21 using clusters with a 5-Hz bandwidth and a 0.5-Hz minimum frequency. The largest vibration amplitudes occur at the second critical speed. The first critical speed can be observed at a

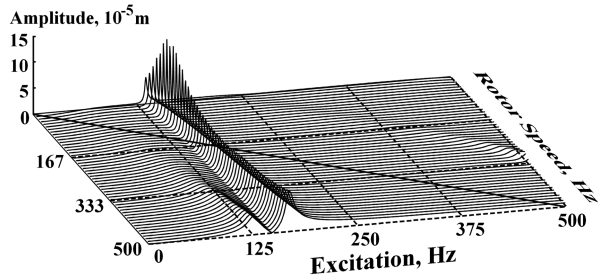

Fig. 11 Spectral map plot of the studied rotor-bearing system.

rotor speed of around 500 Hz with a 125-Hz excitation frequency. The half-frequency whirling can be observed at a rotor speed of approximately 330 Hz with a 500-Hz excitation frequency.

V. Conclusions

A full rotordynamic analysis over the studied single spool gas turbine was successfully performed, taking into account the bearing stiffness and damping dynamics. The rotor-bearing system was specifically designed for this application, including the five-stage axial compressor and the free turbine rotor. The front and rear bearings were carefully designed to impart sufficient stiffness and damping characteristics to the rotor and to avoid the occurrence of critical speeds inside the gas turbine operating speed range.

The numerical analyses revealed interesting aspects of the rotordynamic behavior of the studied gas turbine. We found a severe attenuation of the first critical speed due to the high damping performance of the squeeze film damper. The second critical speed proved to be the most troublesome, although it was found far outside of the operating speed range. Another consequence of the high damping performance of the squeeze film damper is the possible occurrence of a half-frequency whirling; an example of this occurrence can be observed in the spectral map plot. However, under normal operating conditions, this half-frequency whirling is not likely to occur because it arises in the spectral map plot at approximately 330 Hz of rotor speed with a 500-Hz excitation frequency. Unbalance responses of the rotor-bearing system were evaluated in both the five-stage axial compressor and the free turbine rotor. We found acceptable levels of vibration for these components; consequently, blade rub is avoided.

A good agreement among the results could be verified in all numerical analyses. The dynamic behavior of the rotor-bearing system was predicted, and potential vibration problems were avoided. The finite element model was carefully developed, and the numerical analyses were strictly evaluated. Nevertheless, the observations made here from the theoretical results should undergo experimental verification, which was not possible for this study because of the unavailability of the test rig.

Acknowledgments

The authors would like to thank FINEP FNDCT 01.04.1045.00, CNPq 385582/2006-4 and the Reference Center for Gas Turbines for their financial support.

References

[1] Kalita, M., and Kakoty, S. K., "Analysis of Whirl Speeds for Rotor-Bearing Systems Supported on Fluid Film Bearings," *Mechanical Systems and Signal Processing*, Vol. 18, No. 6, 2004, pp. 1369–1380. doi:10.1016/j.ymssp.2003.09.002

[2] Chiang, H-W. D., Hsu, C-N., and Tu, S-H., "Rotor-Bearing Analysis for Turbomachinery Single- and Dual-Rotor Systems," *Journal of Propulsion and Power*, Vol. 20, No. 6, 2004, pp. 1096–1104. doi:10.2514/1.3133

[3] Jeon, S. M., Kwak, H. D., Yoon, S. H., and Kim, J., "Rotordynamic Analysis of a Turbopump with the Casing Structural Flexibility," *Journal of Propulsion and Power*, Vol. 24, No. 3, 2008, PP. 433–436. doi:10.2514/1.33551

[4] Combescure, D., and Lazarus, A., "Refined Finite Element Modelling for the Vibration Analysis of Large Rotating Machines: Application to the Gas Turbine Modular Helium Reactor Power Convertion Unit," *Journal of Sound and Vibration*, Vol. 318, Nos. 4–5, 2008, pp. 1262–1280. doi:10.1016/j.jsv.2008.04.025

[5] Zorzi, E. S., and Nelson, H. D., "Finite Element Simulation of Rotor-Bearing Systems with Internal Damping," *Journal of Engineering for Power*, Vol. 99, No. 1, 1977, pp. 71–76. doi:10.1115/1.3446254

[6] Ferraris, B. G., and Lalanne, M., "Rotordynamics Prediction in Engineering," Wiley, New York, 1998.

[7] Genta, G., "Vibration of Structures and Machines: Practical Aspects," Springer, New York, 1999.

[8] Chen, W. J., and Gunter, E. J., "Introduction to Dynamics of Rotor-Bearing Systems," Trafford Publishing, Bloomington, IN, 2005.

[9] Creci, G., Menezes, J. C., Monteiro, J. F. C., and Corrá, J. A., "Investigation into the Dynamic Behaviour of a Lubricated Radial Ball Bearing Using the EHL Contact Theory," *Proceedings of the 8th Brazilian Conference on Dynamics, Control and Applications*, Sociedade Brasileira de Matemática Aplicada e Computacional, Belo Horizonte, Brazil, 2009.

[10] Creci, G., Menezes, J. C., Monteiro, J. F. C., and Corrá, J. A., "Dynamic Characteristics of an Unsealed Squeeze Film Damper with a Circumferential Feeding Groove," *Proceedings of the 20th International Congress of Mechanical Engineering*, Associação Brasileira de Engenharia e Ciências Mecânicas, Rio de Janeiro, Brazil, 2009.

[11] Genta, G., "On a persistent Misunderstanding of the role of Hysteretic Damping in Rotordynamics," *Journal of Vibration and Acoustics*, Vol. 126, No. 3, 2004, pp. 459–461. doi:10.1115/1.1759694

F. Liu
Associate Editor